

Open-state structure of veratridine-activated human $\text{Na}_v1.7$ reveals the molecular choreography of fast inactivation

Xiao Fan^{1,4,5}, Jiaofeng Chen^{2,4}, Lingfeng Xue^{3,4}, Huan Wang², Tong Wu², Xiaoshuang Huang¹, Fangzhou Lu¹, Xueqin Jin², Chen Song^{3,5}, Jian Huang^{1,5}, and Nieng Yan^{1,2,5}

¹Institute of Bio-Architecture and Bio-Interactions (IBABI), Shenzhen Medical Academy of Research and Translation, Guangming District, Shenzhen 518107, Guangdong, China

²Beijing Frontier Research Center for Biological Structures, State Key Laboratory of Membrane Biology, Tsinghua-Peking Joint Center for Life Sciences, School of Life Sciences, Tsinghua University, Beijing 100084, China

³Center for Quantitative Biology, Academy for Advanced Interdisciplinary Studies, Peking University, Beijing 100871, China

⁴These authors contribute equally.

⁵To whom correspondence should be addressed: Nieng Yan (nyan@tsinghua.edu.cn), Jian Huang (huangjian@smart.org.cn), Chen Song (c.song@pku.edu.cn), and Xiao Fan (xfan@smart.org.cn).

Abstract

Almost all the reported cryo-EM structures of eukaryotic voltage-gated sodium (Na_v) channels, including those of human $\text{Na}_v1.1$ - $\text{Na}_v1.8$, represent various inactivated states that are characteristic of non-conductive pore domain (PD) and voltage-sensing domains (VSDs) activated to varying degrees. To capture an open-state Na_v structure, we treated purified human $\text{Na}_v1.7$ with veratridine (VTD) and solved its cryo-EM structures. Two VTD-bound $\text{Na}_v1.7$ complexes were obtained. One, with VTD inserted in the IFM-binding corner (site I), resembles other inactivated structures. The other, wherein VTD traverses the central cavity (site C), represents an activated conformation with a diameter of 8.2 Å at the constriction site of the intracellular gate. Structural analysis reveals the mechanism of action of VTD's bimodal modulation of Na_v channels. More importantly, a comparison between this open state and inactivated structures provides detailed molecular insight into the fast inactivation process.

Introduction

In multicellular organisms, electrical signaling is indispensable for nearly all neuronal activities and a wide range of physiological processes ¹⁻³. Voltage-gated sodium (Na_v) channels govern the initiation and transmission of electrical signals in the form of action potentials in excitable systems such as neurons and muscles. Na_v channels activate upon membrane depolarization, followed by fast inactivation to ensure the repetitive firing of action potentials ¹⁻³. Following decades of rigorous investigation into their physiological and pathophysiological roles, recent research focus has mainly been on elucidating the structure-function relationship of Na_v channels, as the technological breakthrough in single-particle cryo-electron microscopy (cryo-EM) has led to structural determination of human $\text{Na}_v1.1$ - $\text{Na}_v1.8$ ³⁻⁸.

Despite the rapid progress in the structural pursuit of Na_v channels, most of the mammalian Na_v structures captured to date represent inactivated states, characteristic of non-conductive pore domain (PD), depolarized or up voltage-sensing domains (VSDs), and the fast inactivation motif, Ile/Phe/Met (IFM), wedged in the receptor site adjacent to the intracellular gate ³. Towards an in-depth and comprehensive understanding of their working mechanisms, structural snapshots of Na_v channels in all major states are indispensable. As of now, the structure of Na_v channels in the activated or resting state is yet to be determined.

Many strategies have been employed to lock the purified Na_v channels in distinct conformations. Certain peptide toxins successfully trap VSD_{IV} in a down conformation, but the other three VSDs and PD remain unchanged^{9,10}. One structure of a rat $\text{Na}_v1.5$ mutant r $\text{Na}_v1.5$ -QQQ, in which the IFM motif was replaced by Gln/Gln/Gln, was described as the open state in the presence of the open-pore blocker propafenone¹¹. However, there is a key mismatch between the structural model and the 3D EM reconstruction (Fig. S1). As will be elaborated later, our molecular dynamics simulation (MDS) analysis of the original and corrected structures of r $\text{Na}_v1.5$ -QQQ suggested that neither could be conductive.

To further probe Na_v gating transitions, we engineered a series of point mutations to modulate the voltage dependence of activation and inactivation of $\text{Na}_v1.7$ channels^{12,13}. In the structure of $\text{Na}_v1.7\text{M11}$, a mutant that contains eleven rationally designed single point mutations, VSD_1 displays a completely down conformation and the PD is in a tightly contracted state, lacking the fenestrations seen in other inactivated Na_v structures¹². Electrophysiological characterizations suggest that the structure of $\text{Na}_v1.7\text{M11}$ may represent a closed-state inactivation (CSI) conformation. The structural study of $\text{Na}_v1.7\text{M11}$ demonstrates the feasibility of capturing $\text{Na}_v1.7$ in distinct functional states. In fact, $\text{Na}_v1.7$ has been more extensively characterized structurally than other subtypes, due in part to well-established evidence linking it to pain sensation and subsequent drug development efforts targeting it for analgesic relief¹⁴⁻¹⁷. Since 2019, more than twenty human $\text{Na}_v1.7$ structures

have been determined in complex with diverse modulators^{3,12,13,18-23}. $\text{Na}_v1.7$ also yields the highest resolution for any Na_v structures, at 2.2 Å for the overall structure¹⁹.

Encouraged by these successes, we continued to focus on human $\text{Na}_v1.7$ with the goal of determining its structures in both resting and activated states. In an attempt to determine the structure of $\text{Na}_v1.7$ in the activated state, we treated the channel with veratridine (VTD), an alkaloid neurotoxin derived from the lily family known to act as a potent Na_v opener²⁴⁻²⁶. Here, we report the cryo-EM structures of wild-type (WT) $\text{Na}_v1.7$ in distinct VTD-bound conformations. The structure of $\text{Na}_v1.7$ with VTD standing near the IFM motif, defined as site I (I for inactivation), is reminiscent of the cannabidiol (CBD)-bound, inactivated state²². The other structure, where the elongated steroidal alkaloid VTD traverses the spacious cavity of the PD (site C), appears to represent the activated state with all four VSDs in the up state and the pore conductive, as verified by the MDS analysis. Structural comparison of $\text{Na}_v1.7$ in the activated and inactivated states elucidates the dynamic details underlying fast inactivation and affords the molecular basis for dozens of disease-related mutations.

Results

Distinct structures of $\text{Na}_v1.7$ treated with VTD

Veratridine (VTD) has long been recognized as a classical sodium channel opener, yet its precise mechanism of action (MOA) remains unclear. We therefore sought to solve the structure of VTD in complex with human $\text{Na}_v1.7$. Prior to structural determination, we validated the functional effects of the purchased VTD. Human $\text{Na}_v1.7$ was transiently

expressed in HEK293T cells for whole-cell patch-clamp electrophysiological recordings treated with increasing concentrations of VTD. Under standard steady-state activation and inactivation protocols (see Methods), VTD induced a pronounced hyperpolarizing shift in both activation and inactivation curves (Fig. S1 and Tables S1 and S2), while concurrently suppressing the peak current amplitude in a dose-dependent manner, with an IC_{50} of $92.7 \pm 18.4 \mu\text{M}$ (Fig. 1A). In parallel, VTD elicited a persistent inward current and a prominent tail current, both of which increased with rising concentrations of VTD (Fig. 1A, *left*). To amplify these small-amplitude currents and probe VTD's use-dependent modulation, we applied a 5-Hz pulse protocol. Upon repetitive depolarizations, VTD produced cumulative peak current inhibition and enhanced tail current induction, yielding an EC_{50} for the tail current of $95.4 \pm 16.6 \mu\text{M}$ (Fig. 1A, *middle and right*). The distinctive bimodal modulation of simultaneous suppression of peak current and facilitation of persistent and tail currents is consistent with the reported gating effects of VTD on Na_v channels²⁷.

For structural determination, we co-expressed human $\text{Na}_v1.7$ with auxiliary $\beta 1$ and $\beta 2$ subunits and conducted protein purification and cryo-sample preparation following an established workflow^{12,18}. Considering the limited solubility, VTD was included throughout the purification process to ensure sufficient channel occupancy. When VTD was applied at 100 μM , three major classes were obtained after cryo-EM data acquisition and processing (Figs. S2 and S3 and Table S3). One class has no density corresponding to the ligand, representing an apo form that is identical to the reported wild-type (WT) structure^{12,19} (Fig.

S3E). In another class, the density that clearly belongs to a VTD molecule stands next to the IFM motif (**Figs. S3D and S4**). The overall structure remains similar to the apo channel, with a root-mean-square deviation of 0.96 Å over 1244 C α atoms in the α subunit when compared in PyMol²⁸ (**Fig. 1B**). Local shifts occur in the cytosolic tip of S6_{III} as a result of the insertion of the VTD molecule (**Fig. 1B, right**). Based on our recently proposed definition for ligand binding sites on Na_v and Ca_v channels, this VTD binds to site I (I for inactivation)^{21,29}. We refer to this structure as Na_v1.7V_I, which features an inactivated state.

The last class displays marked deviations in VTD binding and channel conformation. The elongated VTD molecule traverses the entire central cavity (site C), with its 4,9-epoxycevan and 3,4-dimethoxybenzoate ends pointing to fenestrations I-II and III-IV, respectively (**Fig. 1C**). We will call this structure Na_v1.7V_O. As will be demonstrated later, the intracellular gate is widened enough to conduct Na⁺ in this conformation. Unlike CBD, lacosamide, and lamotrigine, each simultaneously binding to two sites on the PD²¹⁻²³, the pore conformations in Class I and Class O are different, suggesting exclusive binding of VTD to site I or site C.

One VTD binding pose is similar to that of CBD at site I

The overall structure of Na_v1.7V_Class I is similar to the CBD-bound one, with an RMSD of 0.92 Å over 1239 C α atoms²⁸ (**Figs. 2A and S4A**). As aforementioned, two CBD molecules simultaneously bind to the PD of Na_v1.7, one inserting into the fenestration (site F) and the

other fortifying the IFM binding site by standing next to Ile and Phe²². In Na_v1.7V_I, only one VTD is observed in the PD. The 3,4-dimethoxybenzoate moiety of the VTD molecule inserts into the corner enclosed by S4-5_{III}, S6_{III}, and S6_{IV}, surrounded mostly by hydrophobic residues. The remaining portion of the molecule, containing the cevanine skeleton, protrudes toward the cytosol (Fig. 2A and 2B). This binding pose is compatible with its higher aqueous solubility conferred by several hydroxy groups.

Both VTD and CBD reduce the peak currents and stabilize the inactivated state, the latter manifested by the leftward shift of the voltage-dependence for steady state inactivation (Fig. S1)²². We reasoned that VTD binding to site I, similar to CBD, might underscore its inhibitory effect on Na_v1.7.

Binding of VTD to site C opens the intracellular gate

In Na_v1.7V_O, VTD, along its long axis, is closer to repeats II and III (Fig. 3A, *left panel*). The molecule is coordinated through extensive hydrophobic and polar interactions. S6_{III} engages four residues, Ser1445, Thr1448, Leu1449, and Phe1452, more than any other individual segments (Figs. 3A and S4B). Leu393 and Ile397 on S6_I, Leu960 on S6_{II}, Trp1332 on S5_{III}, and Ile1745 on S6_{IV} contribute to the van der Waals contacts with VTD. The C-terminal residues of the P1 helices in repeat I-III, Thr359, Cys925, and Ala1403, all use their backbone carbonyl oxygen to hydrogen (H)-bonded with the hydroxy groups of VTD.

Phe1405 on the selectivity filter (SF) loop in repeat III also participates in VTD binding (Fig. 3A, *right panels*).

The PD of Na_v1.7V_O is evidently dilated. Calculation of the radii of the permeation path reveals a diameter of 8.2 Å at the constriction site, sufficient to permeate a 7.2-Å hydrated Na⁺ (Fig. 3B). By comparison, the gate for WT apo channel is 5.0 Å (Fig. 3B). Previously, structural study of rNa_v1.5-QQQ suggested a dialted gate (Fig. 3B). However, re-examination of its deposited map (EMD-31519) and structural coordinates (PDB: 7FBS) revealed an error in model building (Fig. S5). An incorrectly assigned π -helix at segments S_I:400-403 induces a positional shift of all the residues downstream of Gly401, resulting in inaccurate analysis of the permeation path (Fig. S5A).

We rebuilt and refined the PD of rNa_v1.5-QQQ against the deposited map. The updated coordinates (rNa_v1.5-QQQ-rebuilt) substantially improved model fitting to the density map and enhanced model quality metrics across all validation parameters (Fig. S5D). In rNa_v1.5-QQQ-rebuilt, the segment S_I:390-429 shows an RMSD of 3.3 Å over 40 C α atoms compared to the original model, while the rest of the PD remains nearly identical, with an RMSD of 0.4 Å over 542 C α atoms. The gate diameter of the rebuilt model is 5.6 Å, slightly smaller than that of the original model, 6.2 Å (Fig. S5E). The rebuilt rNa_v1.5-QQQ model will be used for all major comparisons and analyses unless otherwise stated.

HOLE analysis confirms that, among all publicly available Na_v structures, $\text{Na}_v1.7V_O$ presented in this study is the only one with the gate diameter large enough to potentially allow permeation of hydrated Na^+ . We will present the molecular dynamics simulation (MDS) confirmation of the open pore in the next section.

The two classes of VTD-bound structures can be superimposed with an RMSD of 1.2 Å over 1180 $\text{C}\alpha$ pairs. Despite the prominent structural deviations of the PD segments, most of the VTD-coordinating residues remain nearly unchanged at site C, except those on S6_{III}. Notably, Thr1448 and Leu1449 displaced to avoid a steric clash with VTD, suggesting these residues are critical for coupling VTD binding at site C to pore opening (Fig. 3C).

The gate is conductive in $\text{Na}_v1.7V_O$

In the 3D EM map of $\text{Na}_v1.7V_O$, residues 1465-1497, which correspond to the IFM-containing III-IV linker, are completely invisible. Compared to the IFM-loaded apo $\text{Na}_v1.7$ structure, the fenestration on the interface of repeats III and IV is directly connected to the intracellular gate, leaving a wide cleft (Fig. 4A). We performed MDS to examine if the substantially widened gate is permeable to hydrated Na^+ ions.

The simulations of PDs were conducted under a transmembrane potential of 120 mV. The intracellular gate is fully hydrated in the $\text{Na}_v1.7V_O$ structure. Consistently, ion permeation analysis confirmed the permeation of Na^+ ions with a calculated conductance of

13.8 ± 5.0 pS, which is comparable to the experimental value³⁰ (Fig. 4D). In contrast, the apo WT hNa_v1.7 and the two rNa_v1.5-QQQ (original and rebuilt) structures exhibited minimal hydration at the corresponding region (Figs. 4B and 4C). Neither could permeate Na⁺ ions in our MDS analysis.

We also characterized the dynamic process of Na⁺ permeation through the channel (Fig. 4E). Na⁺ ions remained hydrated as they passed through the intracellular gate. Moreover, trajectory analysis showed that permeating ions followed an asymmetric path, with Na⁺ ions preferentially located near S6_I, S6_{IV}, and the wide cleft between S6_{III} and S6_{IV} (Fig. 4F).

Structural basis for fast inactivation

We previously, in the absence of an open structure, suggested that the IFM motif might execute fast cutoff of the ion flow mainly through pushing S6_{IV} to close the intracellular gate^{7,8}. Determination of a conductive structure of Na_v1.7 fills up a critical void in the process of fast inactivation and offers an updated view on the cascade of molecular events that complete the fast inactivation in Na_v channels.

When the structures of Na_v1.7V_O and the apo channel are overlaid, there is nearly no change in their VSDs, all of which exhibit the depolarized or up conformations (Fig. 5A, left). By contrast, the S5 and S6 segments and the S4-5 constriction ring in all four repeats

undergo structural changes to varying degrees (**Fig. 5A, right**). In all the available Na_v structures, including $\text{Na}_v1.7\text{V}_-\text{O}$, the SF and its supporting P1, P2, and the upper halves of S5 and S6 segments remain rigid (**Fig. 5B**). We will hereafter refer this region as the PD shoulder.

Superimposition of $\text{Na}_v1.7\text{V}_-\text{O}$ and the apo structures relative to the shoulder shows tilt of the S6 segments in repeats II-IV, all starting around the fourth helical turn. Note that in repeats I-III, a conserved Gly is positioned on this helical turn, likely representing the key residue to provide the flexibility for the downstream segment (**Fig. 5B**). At first sight, the cytosolic half of S6_{III} undergoes the most marked displacement, with the $\text{C}\alpha$ atom of the cytosolic tip moving by 8.0 Å; those of S6_{IV} and S6_{II} are displaced by 4.5 Å and 4.3 Å, respectively; S6_I seems to be nearly unchanged (**Fig. 5A, right**). Interestingly, detailed inspection shows that the fourth helical turn in S6_I undergoes an $\alpha \rightarrow \pi$ relaxation from the open to the inactivated state, an important structural shift that reorganizes the inner wall of the pore cavity (**Fig. 5B**).

Then what are the determinants that lead to the structural re-arrangement of the pore-forming segments? When the IFM motif is accessing the acceptor site, the Phe residue, which would clash with Asn1753 and Ile1756 on S6_{IV}, directly pushes Ile1756 toward the S6_I segment (**Fig. 5C, upper inset**). Meanwhile, the dragging force exerted by the shift of the III-IV helix, a process that was analyzed by us and others previously^{7,10,31}, and the van der

Waals attraction of Phe1460 on S6_{III} to the Ile and Phe residues in IFM pulls the cytoplasmic terminus of S6_{III} toward S6_{IV}.

The displacements of S6_{III} and S6_{IV} have a profound effect on the pore conformation. Concerted pushing of S6_{IV} and pulling of S6_{III} collectively narrows the intracellular gate, making it impermeable to Na⁺ ions (*Fig. 5A, right*). The side cleft between S6_{III} and S6_{IV} in the open pore is now stitched by an array of hydrophobic residues, only leaving a small fenestration on the interface of repeats III and IV (*Fig. 5D, left*). On the other side of S6_{IV}, the displacement of residues Val1758 and Ile1759 would clash with Ile394 and Leu398 on S6_I, respectively, if there were no additional conformational changes. The $\alpha \rightarrow \pi$ helical transition in the middle turn of S6_I affords the solution. The rotation of the ensuing S6_I segment turns the bulky hydrophobic chains of Ile394 and Leu398 away, repositioning Ala399 to interact with Ile1759. Another consequence of the $\alpha \rightarrow \pi$ shift is to re-orient Phe391 to interact with Tyr1755, further shrinking the volume of the central cavity (*Fig. 5D, right*). The concomitant events accompanying the formation of the IFM binding site and its binding to this site quickly stops ion flow at the narrowed gate.

The above analysis shows that both S6_{III} and S6_{IV} only undergo swing motions, without axial rotation, to close the gate. However, the “apo” channel, like in most other Na_V structures, has a glyco-diosgenin (GDN)-like density penetrating the intracellular gate. We previously analyzed in detail that this conformation, despite having a non-conductive gate,

appears to be less ideal for IFM accommodation due to positioning a polar residue Asn1753 adjacent to the hydrophobic Phe residue from IFM¹⁹ (**Fig. 5C, insets**). We have also observed that the S6_{IV} segment tends to adopt the π form in the presence of channel antagonists, such as Protoxin II (ProTx-II), Huwentoxin IV, and a number of small-molecule inhibitors^{19,21-23}. We have shown in detail that the simple $\alpha \rightarrow \pi$ transition of the single segment S6_{IV} has multiple consequences, including reshaping the IFM-binding site to a more compatible hydrophobic cavity, further tightening the intracellular gate to an extent that is too narrow for GDN binding, and closing or shrinking the III-IV and IV-I fenestrations¹⁹.

When the PD structures of Na_v1.7V_O and the ProTx-II bound Na_v1.7 are superimposed relative to the shoulder, the $\alpha \rightarrow \pi$ rotation in the middle of S6_{IV} is evident (**Fig. 5E, upper**). Consequently, while the Phe in IFM pushes Asn1753 and Ile1756 away, it also attracts Met1754 to revolve toward the hydrophobic cluster formed by Phe1460, Ile and Phe in the IFM motif (**Fig. 5E, lower**). And these effects would reduce the overall binding affinity of the IFM motif, rendering the channel less prone to inactivation.

Discussion

The structural analyses presented here reveal the molecular foundation for the dual actions of VTD on Na_v channels. Binding to site I stabilizes an inactivated state, consistent with the left shift of the steady-state inactivation curve when the channels are treated with VTD (**Fig. S1**). Inhibition of the peak currents is likely a collective result of VTD binding to both sites, and

site C binding may be responsible for the use-dependence of peak current inhibition as well as the induced persistent currents (Fig. 1A).

The binding pose of VTD at site C is consistent with the reported observation in single-channel recording that VTD led to reduced conductance yet increased open probability of the Na_v channel^{32,33}. Channel opening may be induced when VTD is accessing site C. Then, where is the entry site? The use-dependent channel inhibition and opening by VTD, along with the proximity of its 3,4-dimethoxybenzoate end to S6_{III} in both binding poses, suggest that VTD may initially bind to site I and then travel to site C during the intracellular gate opening. However, we cannot exclude the possibility that VTD may approach the cavity from the fenestrations or the intracellular gate. Addressing this question requires comprehensive characterizations. The static structures reported here set the framework for future computational and experimental analyses.

Uniform or diverse PD conformations in fast inactivation?

Prior to the determination of an open Na_v structure in this study, the PD has mainly displayed three non-conductive conformations among the dozens of eukaryotic Na_v structures, tight, relaxed, and loose. The PD in Na_vPaS and $\text{Na}_v1.7\text{-M11}$ represent the most contracted conformation, wherein the diameter of the intracellular gate is less than 2 Å^{6,12,34}. This sealed gate cannot accommodate any lipid. In a relaxed PD, exemplified by the “π-form” of the ProTx-II and HWTX-IV bound $\text{Na}_v1.7$, the constriction site is less than 3 Å in diameter, still

disallowing the penetration of a steroid-like molecule¹⁹. In the majority of the Na_v structures, the intracellular gate, with a diameter between 5-6 Å, is penetrated with a GDN-like molecule, and we refer to this state as the loose PD. Note that three similar states of the PD have been observed in Ca_v channels, although the detailed parameters, such as the gate diameter and the α or π form of the S6 segments, vary³⁵.

$\text{Na}_v1.7\text{-M11}$, with its tight PD and one down VSD, may represent the conformation of the closed-state inactivation. Then does the tight PD resemble that in the resting channels? To answer this question, a bona fide resting-state structure is necessitated. By contrast, all four VSDs are up in the Na_v structures with relaxed or loose PD³. Then, which represents the fast inactivated conformation, the relaxed, the loose, or both? We previously suggested that the relaxed state, in which the chemical environment is more compatible with IFM insertion, may reflect the fast inactivated state. Yet, a key question concerns the steroid-like molecule in the intracellular gate in the loose conformation. If the density is only from a GDN or a cholesterol hemisuccinate, which were supplemented in high concentration during channel purification, such conformation is in essence an artifact. However, is it possible that a cholesterol or steroid molecule may penetrate into the gate even under physiological conditions? If so, how quick can it occur? Is it related to slow inactivation? It is noted that a recent study suggested that fast inactivation might involve rotation of the S6_{III} and S6_{IV} segments. Although no rotation of S6_{III} is observed when the structures of the open and relaxed channels are compared, the S6_{IV} segment does undergo an $\alpha \rightarrow \pi$ transition in addition

to the swing motion of the helix. This observation further supports that the relaxed conformation may correspond to the fast inactivated state.

Disease mutations mapped to the inactivation segments

Unlike the canonical “ball-and-chain” model, our structural comparison supports the “door wedge” mechanism, in which docking of the IFM motif into its receptor site allosterically drives pore closure. During fast inactivation, dissociation of the III–IV linker from the CTD becomes essential, enabling its engagement with the S4–5 linker in repeat IV and ultimately driving IFM motif binding to its receptor site (Fig. 5F).

Mapping pathogenic mutations across Na_v channel subtypes onto these structures establishes a unified framework for interpreting diverse channelopathies. Dozens of mutations cluster either at the interfaces between the IFM motif-bearing III-IV linker and its receptor site or within residues that mediated the conformational transitions underlying inactivation (Fig. 5G). These hotspots are linked to a broad spectrum of channelopathies, including epileptic encephalopathies, Dravet syndrome (DRVT), Long QT syndrome 3 (LQT3), Brugada syndrome 1 (BrS1), and pain disorders such as primary erythromelalgia (PERYTHM) and paroxysmal extreme pain disorder (PEXPD).

Within the context of our “door wedge” model, two mechanistic classes of mutations emerge. Mutations that weaken IFM-receptor interactions directly compromise the fast

inactivation, whereas those that hinder the conformational coupling required for pore closure influence the process indirectly. Both perturbations would enhance channel opening during prolonged depolarization, resulting in a depolarizing shift in steady-state inactivation, enhanced persistent or tail currents, and accelerated recovery from inactivation.

Consistent with this hypothesis, LQT3 mutations such as F1486del and F1486L in $\text{Na}_v1.5$ ³⁶, located within the IFM motif itself, markedly impair inactivation and increase late I_{Na} . Similarly, F1473C/S in $\text{Na}_v1.5$ (equivalent to F1460V in $\text{Na}_v1.7$) causes pronounced QT prolongation, elevated late I_{Na} , a rightward shift of steady-state inactivation, and faster recovery from inactivation³⁷. Several glycine residues flanking the N-terminus side of the IFM motif appear to confer flexibility of the inactivation particle movement; substitutions such as G1489K in $\text{Na}_v1.1$ (equivalent to G1476K in $\text{Na}_v1.5$) or G1481V/E in $\text{Na}_v1.5$ accelerate recovery from fast inactivation and increase late I_{Na} ³⁷, consistent with impaired IFM docking.

Our open-state structure further identifies coupling residues—Asn395, Leu398, Tyr1755, and Ile1756—situated within the IV-I fenestration of $\text{Na}_v1.7$. Mutations at these positions, corresponding to N406K/S, L409V, Y1767C, and I1768V in $\text{Na}_v1.5$, underlie LQT3 phenotypes³⁸⁻⁴¹. Notably, Y1767C and N406K promote elevated late I_{Na} , and all these mutations accelerate recovery from inactivation compared with WT channels, suggesting destabilization of the inactivated state.

Together, these findings establish a unifying mechanistic framework in which disruption of IFM-mediated coupling compromises fast inactivation and provides a structural basis for a broad range of Na_v channelopathies.

Acknowledgements

We thank the cryo-EM facility at Princeton Imaging and Analysis Centre for technical support. This work was funded by the National Natural Science Foundation of China (32271252 to N.Y. and 32501081 to J.H.). N.Y. was supported by the Shirley M. Tilghman endowed professorship from Princeton University from 2017 to 2022. X.F. has been supported by the HFSP long-term fellowship (LT000754/2020-L) from the International Human Frontier Science Program Organization (HFSPO) from 2020 to 2023. J.H. and X.F. are supported by the start-up funding from Shenzhen Medical Academy of Research and Translation (SMART).

Author Contributions

N.Y., J.H., and X.F. conceived the project. X.F., J.C., L.X., H.W., T.W., X.H., F.L., X.J., C.S., J.H., and N.Y. designed experiments; X.F. and J.H. performed all experiments related to cryo-EM studies, including protein expression, purification, and 3D reconstructions; J.C. carried out experiments related to electrophysiology; L.X. performed molecular dynamics simulations; X.H. and F.L. prepared the mutation plasmids; X.F., J.C., L.X., H.W., T.W., X.H., F.L., X.J., C.S., J.H., and N.Y. discussed and analyzed data; X.F., J.H., and N.Y. wrote the manuscript with input from all authors. All authors approved the final manuscript.

Competing interests

The authors declare no competing interests.

Figure Legends

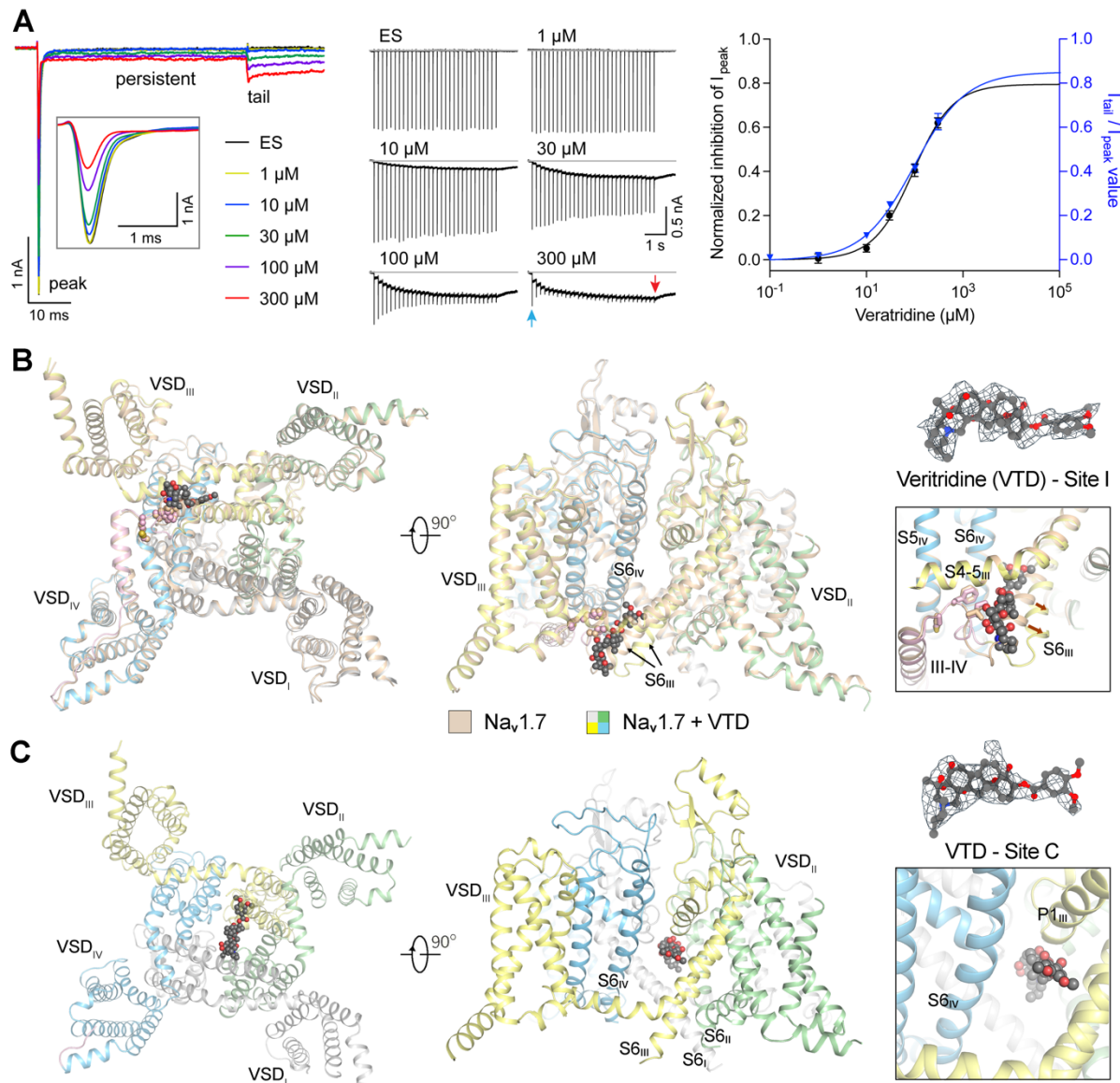


Figure 1 | Bimodal regulation of Na_v1.7 by veratridine may be explained by the dual binding poses on the pore domain. (A) Use-dependent inhibition of Na_v1.7 peak current and enhancement of its tail current by veratridine (VTD). *Left:* Representative traces showing the effects of indicated concentrations of VTD on Na_v1.7 peak, persistent, and tail currents. Cells were held at -120 mV and depolarized to a test pulse to 0 mV for 50 ms. An enlarged view of the peak current is shown in the box. ES, external solution. *Middle:* Representative traces illustrating the use-dependent modulation of VTD on Na_v1.7 currents, evoked by a 5-

Hz train stimulation (30 pulses of 5-ms duration from -120 mV to 0 mV). The accumulated tail current (red arrow) was measured and normalized to the amplitude of the first peak current (blue arrow), with both values corrected against the baseline (grey line). *Right:* Concentration-response relationships for VTD-mediated inhibition of $\text{Na}_v1.7$ peak current (black curve, $\text{IC}_{50} = 92.66 \pm 18.41 \mu\text{M}$, $n = 13, 17, 16, 15, 15$) and enhancement of the accumulated tail current (blue curve, $\text{EC}_{50} = 95.44 \pm 16.62 \mu\text{M}$, $n = 18, 10, 12, 13, 13, 11$). Data are presented as mean \pm SEM. Details are presented in Methods. **(B-C)** Three classes of $\text{Na}_v1.7$ cryo-EM structures were obtained when treated with $100 \mu\text{M}$ VTD, apo and two binding poses for VTD. **(B)** The class I structure, in which a VTD binds next to the fast inactivation Ile/Phe/Met (IFM) motif, is similar to that of the apo-channel. We have named this ligand binding site on Na_v channels the site I. Structures of classes I (colored wheat) and II (colored by repeats) can be superimposed with the root-mean-square deviation (RMSD) of 0.96 \AA over 1244 $\text{C}\alpha$ pairs. The major local shift near site I is highlighted by red arrows in the inset. **(C)** In class O, a VTD traverses the central cavity (site C). The VTD densities, prepared as grey meshes in ChimeraX⁴², are contoured at 6σ . All structure figures, if not otherwise indicated, were prepared in PyMol²⁸.

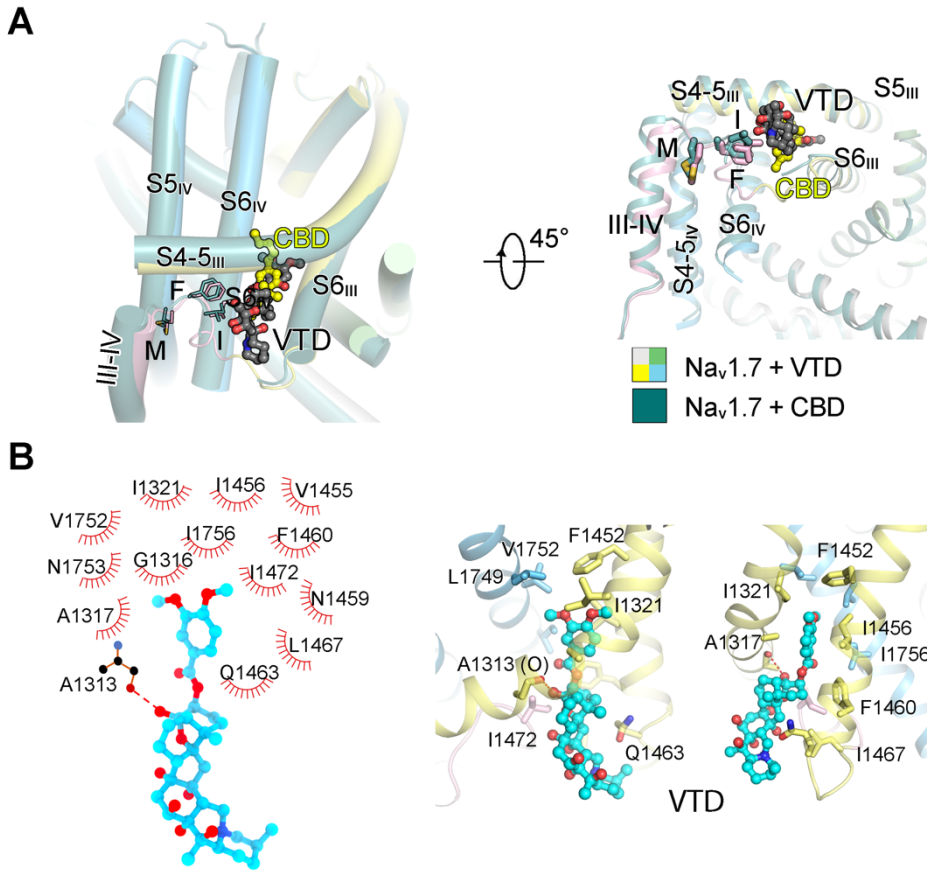


Figure 2 | Site I binding accounts for VTD's antagonistic effect on Na_v channels. (A)

Similar binding poses of VTD and CBD at site I. Structure of VTD (black)-bound Na_v1.7 (Na_v1.7V_Class I) can be superimposed to the CBD (yellow)-bound one with the RMSD of 0.92 Å across all 1239 C_α pairs. A tilt side view and a bottom view of their superimposed pore domain are shown. The IFM motif is shown as sticks. The PDB code for CBD-bound Na_v1.7 is 8G1A. **(B)** Coordinating details of VTD at site I. VTD is shown as cyan ball and sticks, and surrounding residues are shown as sticks. The potential hydrogen bonds are indicated with red dashed lines. *Left*: A schematic illustration of the binding details of VTD at site I. *Middle* and *right*: Two nearly perpendicular side views of the coordination of VTD at site I.

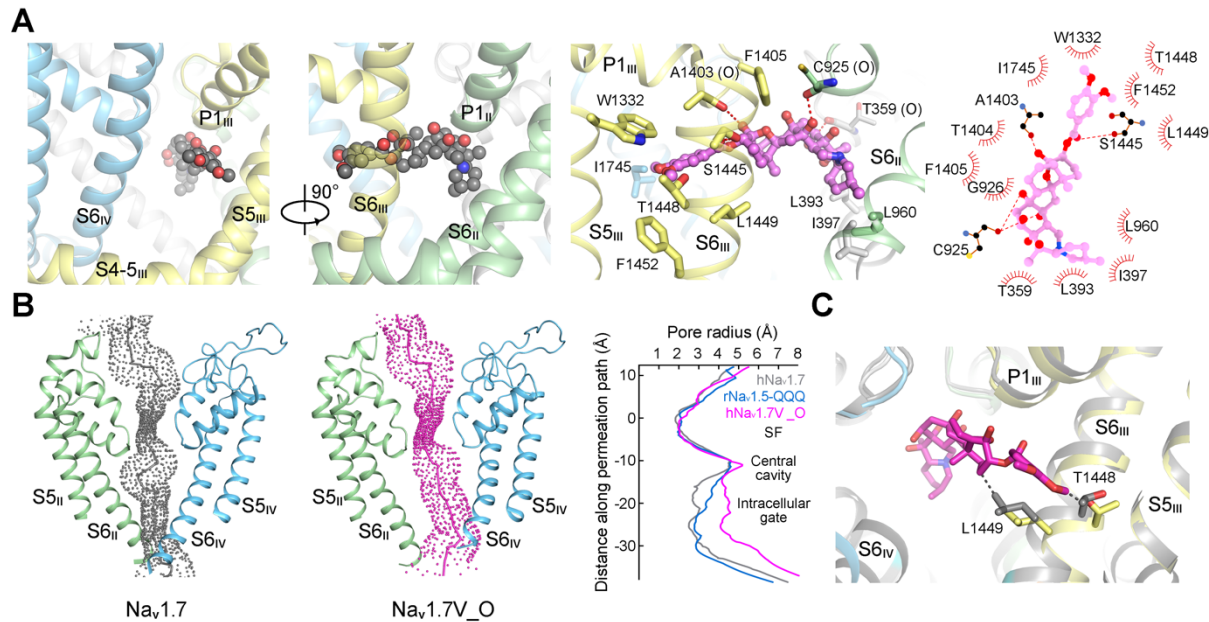


Figure 3 | VTD binding at site C opens the pore. (A) Coordination of VTD in the central cavity. *Left two panels*: Two perpendicular views, in addition to that in Fig. 1c, to illustrate the binding pose of VTD at site C. *Right two panels*: Details of VTD binding. Coordinating residues are shown as sticks. (B) The pore is substantially dilated in the presence of VTD at site C. The permeation path of the pore domain (VTD omitted) is calculated in HOLE⁴³. The radii of the permeation path in the indicated structures are shown on the right. The original error in the model building and the correction of the reported structure r*Na_v1.5*-QQQ is described in Fig. S5. (C) The S6_{III} segment appears to play a major role in coupling pore opening upon VTD binding to site C. VTD would clash with Thr1448 and Leu1449 if S6_{III} had not shifted outward substantially. The black, dashed lines indicate potential clash between VTD groups and the two residues.

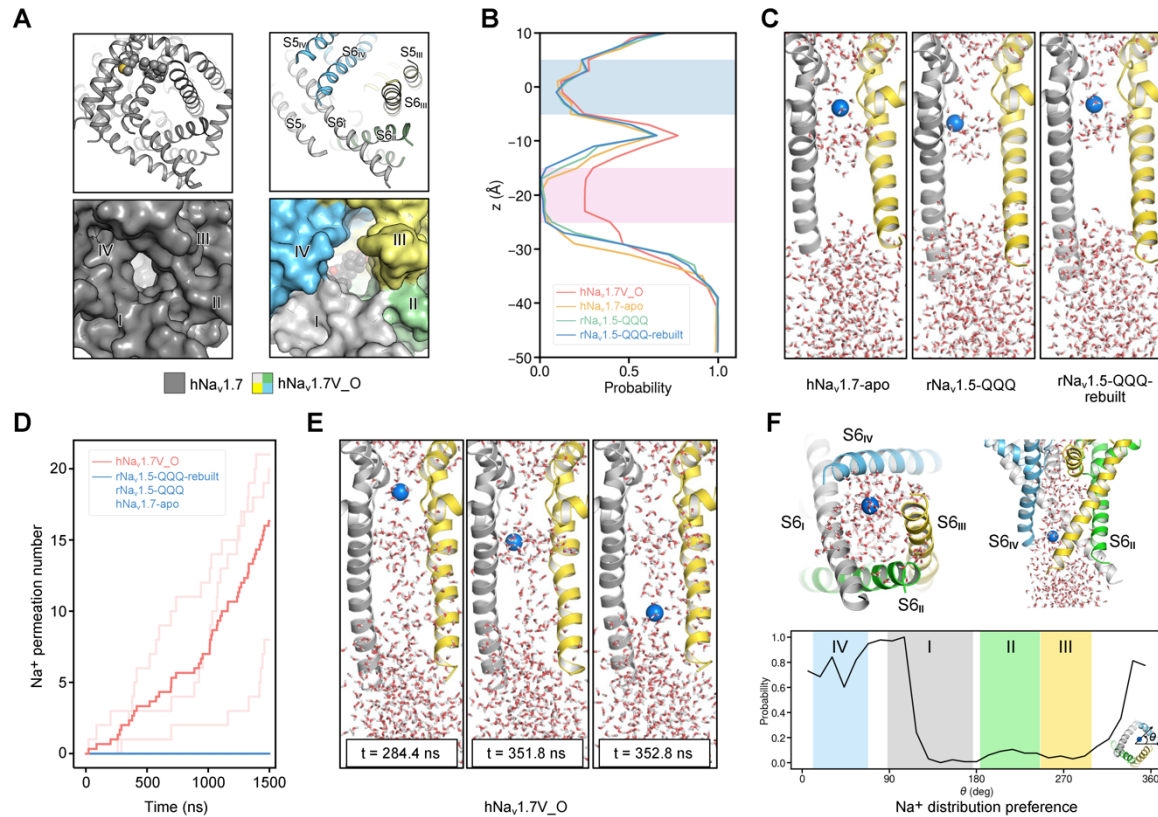


Figure 4 | MD simulation analysis confirms the conductive state of the intracellular gate

in NaV1.7V_O . (A) The intracellular gate opens along the interface of S6_{III} and S6_{IV} . In the structure of NaV1.7V_O , the IFM-containing III-IV linker is invisible. Shown here are identical intracellular views of the PD in the apo and class O structures. (B) Density distribution of water molecules along the z-axis within the central pore of different channel structures. Results are shown for $\text{hNa}_\text{v}1.7\text{V}_\text{O}$ (red), $\text{hNa}_\text{v}1.7$ apo (orange), $\text{rNa}_\text{v}1.5\text{-QQQ}$ (green), and $\text{rNa}_\text{v}1.5\text{-QQQ-rebuilt}$ (blue). Selectivity filter and intracellular gate regions are shaded in blue and pink, respectively. (C) Molecular visualization of the hydration state of different channels. Structures are shown in cartoon representation, with only repeat I and repeat III displayed for clarity. Sodium ions are depicted as blue spheres, and water molecules are shown as red-and-white sticks. (D) Results of ion permeation events. The three

light red lines represent the results of three independent simulations of the hNa_v1.7V_O structure, and the dark red line shows the averaged result. The blue line represents simulation results for the rest three channel structures, where no ion permeation events were observed in three replicate simulations for each case. **(E)** Sequential snapshots of a representative ion permeation event through hNav1.7V_O, with simulation timestamps indicated in each panel. **(F)** Asymmetric distribution of the Na permeation path. *Top:* Snapshots illustrating the angular preference of sodium ions as they permeate through the gate of the hNa_v1.7V_O structure. The left panel presents a bottom view and the right panel displays a side view. *Bottom:* Angular distribution of sodium ions around the four S6 repeats at the gate. The shaded areas represent the angular distributions of residues from repeats I-IV, colored in gray, green, yellow, and blue, respectively. The definition of the angle θ is illustrated at the right corner (see Methods for details).

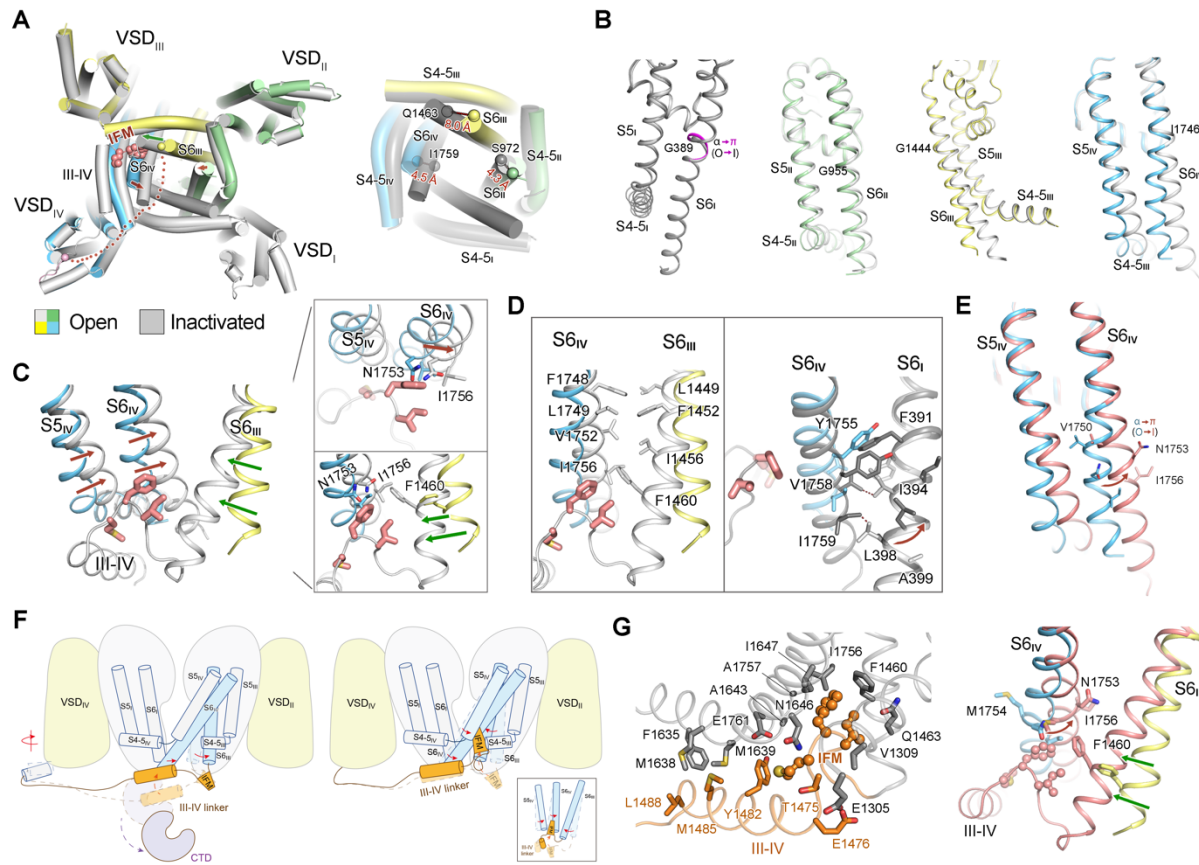


Figure 5 | Structural changes between the open and fast-inactivated $\text{Na}_v1.7$. (A)

Conformational shifts of the S6 and S4-5 segments associated with IFM-induced gate closure. In the open $\text{Na}_v1.7$ structure, the III-IV linker (indicated by the red dotted line), including the IFM motif, is invisible. Structural superimposition of the open and inactivated (PDB code: 7W9K) $\text{Na}_v1.7$ relative to the upper half of the pore domain reveals differential shifts of the S6 and S4-5 segments in the four repeats, as highlighted in the enlarged view on the right. (B) The pore-forming segments in the four repeats undergo distinct shifts to various extent upon fast inactivation. Whereas the cytosolic halves of the S6 segments in repeats II, III, and IV swing to different extents, S6_I has an $\alpha \rightarrow \pi$ transition in its middle helical turn. The deviation locus in each S6 segment is labelled. Structures of the open and inactivated $\text{Na}_v1.7$ are superimposed as in panel A, and the pore-forming segments in the four

repeats are displayed the views that best reflect their respective deviations. **(C)** The IFM motif pulls S6_{III} and pushes S6_{IV} to close the intracellular gate. When the hydrophobic IFM motif wedges into the corner between the S4-5_{III} and S4-5_{IV} segments, it exerts two opposing forces. On one side, a potential clash between the Phe residue with Ile1756 pushes S6_{IV} toward S6_I (upper inset, brown arrows). On the other, it pulls S6_{IV} toward S6_{III} (lower inset, green arrows), resulting in the formation of a hydrophobic core between Ile1756 on S6_{IV} with the Ile and Phe residues in the IFM motif and Phe1460 on S6_{III}. **(D)** Contraction of the pore domain upon fast inactivation. *Left:* The marked shifts of the S6_{III} and S6_{IV} induce their interface rearrangement. As a result, extensive hydrophobic interactions between S6_{III} and S6_{IV} close the wide cleft in the open pore. *Right:* Displacement of S6_{IV} induces the $\alpha \rightarrow \pi$ transition in S6_I to avoid steric clash. Without the rotation following the $\alpha \rightarrow \pi$ transition in S6_I, residues Ile394 and Leu498 would clash with Val1758 and Ile1759 when S6_{IV} is pushed by the IFM motif. **(E)** The π -helical conformation of S6_{IV} provides a more favorable environment for IFM binding at its receptor site, with the polar residue Asn1753 replaced by the hydrophobic Met1754. **(F)** Schematic representation of the ‘door wedge’ allosteric mechanism governing Na_v channel fast inactivation. During fast inactivation, the IFM motif wedges into the corner between the S4-5_{III} and S4-5_{IV} segments, pulling S6_{III} and pushing S6_{IV} to seal the intracellular gate. **(G)** Structural mapping of disease-associated hotspot residues clustered around the IFM motif binding pocket.

Materials and Methods

Whole cell electrophysiology

We applied a protocol similar to our previous publication with minor adjustments⁴⁴⁻⁴⁶. All currents were recorded in HEK293T cells. Cells were transiently co-transfected with human $\text{Na}_v1.7$ and eGFP using lipofectamine 2000 (Invitrogen). Cells with green fluorescence were randomly selected for patch-clamp recordings 24–48 h after transfection. All experiments were performed at room temperature.

Currents were recorded using an EPC10-USB amplifier with Patchmaster software v2*90.2 (HEKA Elektronik), filtered at 3 kHz (low-pass Bessel filter) and sampled at 50 kHz. The borosilicate pipettes (Sutter Instrument) used in all experiments had a resistance of 2-4 $\text{M}\Omega$, series resistance was compensated by >75%. The electrodes were filled with the internal solution composed of 105 mM CsF, 40 mM CsCl, 10 mM NaCl, 10 mM EGTA, and 10 mM HEPES, pH adjusted to 7.4 with CsOH. The external solution contained 140 mM NaCl, 4 mM KCl, 1.5 mM CaCl₂, 1 mM MgCl₂, 10 mM D-glucose, and 10 mM HEPES, pH adjusted to 7.4 with NaOH. The linear component of leaky currents and capacitive transients were subtracted using the P/4 procedure. Only cells with high seal resistance (>1 $\text{G}\Omega$) were used. To investigate veratridine's effects on $\text{Na}_v1.7$, veratridine was dissolved in dimethyl sulfoxide (DMSO; Sigma) to make a stock solution of 100 mM and stored at –20 °C. Working solutions were freshly prepared and perfused to the recording cell using a multichannel perfusion system (VM8, ALA) for several minutes until the pharmacological

effect reached saturation. Prior to drug application, cells were recorded for 5~15 minutes to establish stable peak current.

To assess the inhibitory effect of veratridine on the peak current, cells were held at -120 mV and depolarized to a test pulse to 0 mV for 50 ms. To investigate the use-dependent effect, a train of 30 pulses (5-ms duration to 0 mV) was applied at 5 Hz from a holding potential of -120 mV. The accumulated tail current at the end of the stimulation was normalized to the amplitude of the first peak current. Concentration-response curves were fitted with: $Y = \text{Bottom} + (\text{Top} - \text{Bottom}) / (1 + 10^{((\text{LogIC}_{50}-X) * \text{Hill Slope})})$, where IC_{50} or EC_{50} represents the drug concentration that inhibits 50% of the peak current or activates 50% of the tail current, respectively; X is log of the drug concentration; and Hill Slope is the slope factor.

To characterize channel gating properties, voltage-dependent activation was assessed using a protocol consisting of steps from a holding potential of -120 mV to voltages ranging from -90 mV to +80 mV for 50 ms in 5-mV increments. Conductance (G) was calculated as $G = I / (V - V_r)$, where V_r is the reversal potential. Normalized conductance was plotted against the test voltage (from -90 mV to +30 or +40 mV) to generate activation curves. Voltage-dependent steady-state inactivation was determined with a two-pulse protocol, in which cells were conditioned with 1,000-ms pre-pulses from -130 mV to 0 mV in 5-mV increments, followed by a 50-ms test pulse to 0 mV. Normalized peak currents were plotted against pre-

pulse voltage to construct inactivation curves. Both activation and inactivation relationships were fitted with a Boltzmann function to determine the $V_{1/2}$ and slope factors (k). To ensure data integrity, rigorous quality control criteria were applied, excluding activation curves with slope values (k) ≤ 4 . Data were processed using Fitmaster (HEKA Elektronik), Igor Pro (WaveMetrics), and GraphPad Prism (GraphPad Software). All quantitative data are presented as mean \pm SEM, with n representing the number of independently recorded cells. Statistical significance was assessed using the extra sum-of-squares F test.

Cell culture and transient expression of human $\text{Na}_v1.7$ complex in HEK293F cells

The proteins were expressed using the same codon-optimized constructs from our previous work, specifically human $\text{Na}_v1.7$ (Uniprot Q15858), $\beta 1$ subunit (Uniprot Q07699), and $\beta 2$ subunit (Uniprot O60939) in pCAG expression vector. HEK293F cells (Thermo Fisher Scientific, R79007) were maintained in SMM 293T-II medium (Sino Biological Inc.) at 37 °C under 5% CO_2 and 60% humidity. For transient expression of the human $\text{Na}_v1.7$ complex, each liter culture at a density of $1.5\text{--}2.0 \times 10^6$ cells per mL was transfected with a mixture of 2.5 mg plasmids, including 1.5 mg $\text{Na}_v1.7$, 0.5 mg $\beta 1$, and 0.5 mg $\beta 2$. The plasmid mixture was pre-incubated with 4 mg 40-kDa linear PEI (Polysciences) in 50 ml fresh medium for 15–30 minutes.

Protein purification of human $\text{Na}_v1.7$ -Veratridine complexes

Transfected HEK293F cells (24 L) were harvested \sim 48 h post-transfection by centrifugation at $3,600 \times g$ for 10 min and resuspended in lysis buffer containing 25 mM Tris-HCl (pH 7.5) and 150 mM NaCl. The suspension was supplemented with 0.1 μM veratridine (MCE), 2 mM PMSF, and protease inhibitor cocktail (Selleckchem), followed by incubation at 4 °C with gentle rotation for 30 min. n-Dodecyl- β -D-maltopyranoside (DDM, Anatrace) was then added to a final concentration of 1% (w/v), along with cholestryl hemisuccinate Tris salt (CHS, Anatrace) at 0.1% (w/v). The mixture was incubated at 4 °C for an additional 2 h. The supernatant obtained by centrifugation at $16,000 \times g$ for 45 min was applied to anti-FLAG M2 affinity resin (Sigma) and incubated for batch binding. The resin was washed four times with wash buffer (buffer W) containing 25 mM Tris-HCl (pH 7.5), 150 mM NaCl, 0.06% GDN, 0.1 μM veratridine, and protease inhibitors. Bound proteins were eluted with buffer W supplemented with 0.2 mg mL⁻¹ FLAG peptide (GenScript). The eluent was subsequently passed through Strep-Tactin Sepharose resin (IBA) by gravity flow, washed four times with buffer W, and eluted with buffer W containing 2.5 mM desthiobiotin (IBA). The final eluate was concentrated using a 100-kDa molecular weight cut-off Amicon filter unit (Millipore) and subjected to size-exclusion chromatography on a Superose 6 10/300 GL column (GE Healthcare) pre-equilibrated in buffer containing 25 mM Tris-HCl (pH 7.5), 150 mM NaCl, 0.02% GDN, and 0.1 mM veratridine. The peak fractions were pooled supplemented with 0.5 mM veratridine and incubated at 4 °C for 30 minutes; then concentrated to \sim 10 mg mL⁻¹ for cryo-grid preparation.

Cryo-EM sample preparation and data acquisition

UltrAuFoil (R1.2/1.3 300 mesh, Quantifoil) grids were glow-discharged with easiGlow (PELCO) using 15 mA for 15 s at 0.37 mBar. Vitrobot Mark IV chamber was pre-cooled to 10 °C with 100% humidity. 3 μ l concentrated Na_v1.7-veratridine was applied to freshly treated grid, which was then blotted with filter paper for 4 s and plunged into liquid ethane cooled by liquid nitrogen. Grids were loaded to a 300 kV Titan Krios G3i with spherical aberration (Cs) image corrector (Thermo Fisher). Micrographs were automated recorded in SerialEM by a Gif Quantum K2 Summit camera (Gatan) with 20 eV slit in super-resolution mode at a nominal magnification of 105,000 \times , resulting in a calibrated pixel size of 0.557 Å. Each movie stack was exposed for 5.6 s (0.175 s per frame, 32 frames) with a total electron dose of \sim 50 e⁻/Å². The movie stacks were aligned, summed and dose-weighted using Warp and binned to a pixel size of 1.114 Å per pixel.

Data processing

A total of 5,021 micrographs were collected and preprocessed on-the-fly in Warp⁴⁷, then imported into cryoSPARC⁴⁸. Particles from 100 micrographs were initially auto-picked using blob picking and subjected to 2D classification to generate templates. Class averages displaying clear features were selected for template-based particle picking for the full dataset and *Ab-initio* reconstruction. Picked and extracted bin4 particles were further cleaned via 2D classification to remove obvious junks. The cleaned dataset was subjected to heterogeneous refinement using two initial references derived from *Ab-initio* reconstruction. Bin2 particles

were re-extracted from selected good class, followed by four rounds of heterogeneous refinement and duplicate removal. The best-resolved class was extracted into bin1 for further processing. The selected particles were subjected to two additional rounds of heterogeneous refinement incorporating higher-resolution features. Subsequent non-uniform (NU) refinement of the dominant class, comprising 631,118 particles, yielded a reconstruction at an overall resolution of 2.7 Å. In this reconstruction, the S6_{III} segment exhibited branched density, suggesting a mixed conformational state. To resolve structural heterogeneity, unsupervised 3D classification was performed on the 631,118 particles without providing multiple manually defined references. A range of different initial resolution filters and class numbers, with “force hard classification” enabled, was tried. Classification with a 6 Å low-pass filter and four output classes successfully resolved three distinct conformational states: the open state, the site I-bound state, and the apo-state. The resulting 3D classes were subsequently used as references for heterogeneous refinement, followed by final round of non-uniform refinement. Final reconstructions were obtained at overall resolutions of 2.9 Å for the open state (133,758 particles, 21.2%), 2.7 Å for the site I-bound state (335,177 particles, 53.1%), and 2.9 Å for the apo state (162,183 particles, 25.7%).

Model building and refinement

The published apo-state structure (PDB: 7w9k) was applied as the initial model for hNa_v1.7-veratridine complexes and underwent manual inspection and adjustments in COOT ⁴⁹. The veratridine molecules were then modeled and refined based on the density in COOT ⁴⁹.

Subsequent refinement was performed using the real-space refinement in PHENIX⁵⁰, followed by molecular dynamics-based optimization in ISOLDE⁵¹. A final round of real-space refinement in PHENIX⁵⁰ was conducted to complete and validate the model.

Validation results are detailed in **Table S3**.

Molecular dynamics simulations

The protein models were built with our cryo-EM structures of hNav1.7V_O, hNav1.7 apo, and the previously resolved structure rNav1.5-QQQ (PDB: 7FBS) as well as its rebuilt version. Only the pore domains (residue 233-409, 850-977, 1306-1463, and 1629-1769 in Na_v1.7, and residue 236-429, 824-945, 1320-1481, and 1644-1777 in Na_v1.5) were included in the simulation systems. CHARMM-GUI⁵² was used to build the simulation systems. The protein models were embedded into a POPC lipid bilayer. After membrane insertion, the system was solvated in 0.15 M NaCl solution. The simulation box was around 10×10×12 nm³, which comprised ~120,000 atoms.

We performed MD simulations with GROMACS⁵³ version 2021.2, using the CHARMM36m force field⁵⁴ and CHARMM TIP3P water model. For all the production simulations, the time step was 2 fs. The v-rescale algorithm with a time constant of 0.5 ps was used to maintain the temperature at 310 K⁵⁵, and the Parrinello-Rahman algorithm with a time constant of 5 ps was used to maintain the pressure at 1 bar⁵⁶. The Particle-Mesh Ewald method was used to calculate long-range electrostatics with a cut-off of 1.2 nm⁵⁷, and the van der Waals

interactions were smoothly switched off from 1.0 nm to 1.2 nm. The bonds involving hydrogen were constrained using the LINCS algorithm⁵⁸. The MDAnalysis package⁵⁹ was used to analyze the MD simulation results. PyMOL was used to render molecular visualizations²⁸. The default CHARMM-GUI protocol was used to progressively equilibrate the system, including 5000 steps of energy minimization, 250 ps NVT equilibration, and 1625 ps NPT equilibration. Then we restrained the C α atoms of the protein with a force constant of 1000 kJ/mol/nm² to perform another 100 ns NPT equilibration. For production simulations, we relaxed the restraints of pore helix (10 residues before and after the DEKA locus in the SF), while the C α atoms in other regions were still restrained. We performed ion permeation simulations by applying an electric field of 0.01 V/nm along the pore axis pointing to the intracellular direction, which generated a transmembrane potential of ~120 mV. Three replicates of 1.5 μ s simulations were performed for each simulation system.

Water distribution analysis

The water distribution around the intracellular gate was estimated from production simulation trajectories. The origin was assigned as the mean position of the four C α atoms of DEKA locus and then the pore axis was assigned as the z-axis. By binning the z-axis into 2 \AA grid and calculating the number of water molecules around 1 nm of the pore axis, we obtained the water density distribution along z-axis from the following equation:

$$\rho = \frac{N}{V} = \frac{N}{\pi r^2 \Delta z}$$

where ρ is water density, N is the number of water molecules observed in the cylinder layer, V is the volume of the cylinder layer, $r(=1 \text{ nm})$ is the radius of the cylinder, $\Delta z(=2 \text{ \AA})$ is the grid-spacing. Then the density distribution was normalized by the water density in bulk solution.

Ion permeation analysis

The permeation events were determined by analyzing the z coordinates of ion trajectories: if an ion moved from extracellular side across the membrane to the intracellular side, one permeation event was counted. By counting the number of permeation events, the conductance of the channel for ion (g_{ion}) can be calculated as follows:

$$g_{\text{ion}} = \frac{I}{V} = \frac{N_p Q_{\text{ion}}}{tV} = \frac{N_p Q_{\text{ion}}}{tEL_z}$$

where N_p is the observed number of permeation events, Q_{ion} is the charge of the permeating ion, t is the simulation time, V is the transmembrane potential, E is the applied electric field, and L_z is the box size in the z direction. Errors were estimated by the standard deviations of three replicates.

Angular distribution analysis of permeating ions at the gate

The angular distribution of the permeating ions in the gate region was analyzed to evaluate the asymmetric nature of the permeation pathway. The analysis included ions located within 10 \AA of the pore axis and between $z = -30$ to -15 \AA . The coordinate system used for this analysis was consistent with that employed for the analysis of water distribution. The angle is

defined by two vectors: one vector aligns with the x-axis of the coordinate system, originating from the channel axis and extending parallel to the membrane plane. Then the angle was defined by the vectors from the origin to sodium ions and the x-axis. The second vector extends from the channel axis to the permeating ion, which is also parallel to the membrane plane. In this context, the specific choice of the x-axis is inconsequential. The distribution probability was obtained through normalization using the maximum value of the angular distribution.

Data availability

The data that support this study are available from the corresponding authors upon reasonable request. The cryo-EM maps and corresponding atomic coordinates have been deposited in the Electron Microscopy Data Bank (EMDB) and the Protein Data Bank (PDB).

References:

- 1 Hille, B. *Ion channels of excitable membranes*. 3rd edn, (Sinauer, 2001).
- 2 Hodgkin, A. L. & Huxley, A. F. Resting and action potentials in single nerve fibres. *The Journal of physiology* **104**, 176-195 (1945).
- 3 Huang, J., Pan, X. & Yan, N. Structural biology and molecular pharmacology of voltage-gated ion channels. *Nat Rev Mol Cell Biol* **25**, 904-925 (2024). <https://doi.org/10.1038/s41580-024-00763-7>
- 4 Liao, M., Cao, E., Julius, D. & Cheng, Y. Structure of the TRPV1 ion channel determined by electron cryo-microscopy. *Nature* **504**, 107-112 (2013). <https://doi.org/10.1038/nature12822>
- 5 Kuhlbrandt, W. Biochemistry. The resolution revolution. *Science* **343**, 1443-1444 (2014). <https://doi.org/10.1126/science.1251652>
- 6 Shen, H. et al. Structure of a eukaryotic voltage-gated sodium channel at near-atomic resolution. *Science (New York, N.Y)* **355**, eaal4326 (2017). <https://doi.org/10.1126/science.aal4326>
- 7 Yan, Z. et al. Structure of the Nav1.4-beta1 Complex from Electric Eel. *Cell* **170**, 470-482 e411 (2017). <https://doi.org/10.1016/j.cell.2017.06.039>
- 8 Pan, X. et al. Structure of the human voltage-gated sodium channel Nav1.4 in complex with beta1. *Science (New York, N.Y)* **362** (2018). <https://doi.org/10.1126/science.aau2486>
- 9 Jiang, D. et al. Structural basis for voltage-sensor trapping of the cardiac sodium channel by a deathstalker scorpion toxin. *Nature communications* **12**, 128 (2021). <https://doi.org/10.1038/s41467-020-20078-3>
- 10 Clairfeuille, T. et al. Structural basis of alpha-scorpion toxin action on Nav channels. *Science (New York, N.Y)* **363** (2019). <https://doi.org/10.1126/science.aav8573>
- 11 Jiang, D. et al. Open-state structure and pore gating mechanism of the cardiac sodium channel. *Cell* **184**, 5151-5162.e5111 (2021). <https://doi.org/10.1016/j.cell.2021.08.021>
- 12 Huang, G. et al. Unwinding and spiral sliding of S4 and domain rotation of VSD during the electromechanical coupling in Na(v)1.7. *Proceedings of the National Academy of Sciences of the United States of America* **119**, e2209164119 (2022). <https://doi.org/10.1073/pnas.2209164119>
- 13 Li, Z. et al. Dissection of the structure-function relationship of Na(v) channels. *Proceedings of the National Academy of Sciences of the United States of America* **121**, e2322899121 (2024). <https://doi.org/10.1073/pnas.2322899121>
- 14 Cox, J. J. et al. An SCN9A channelopathy causes congenital inability to experience pain. *Nature* **444**, 894-898 (2006). <https://doi.org/10.1038/nature05413>
- 15 Cummins, T. R., Dib-Hajj, S. D. & Waxman, S. G. Electrophysiological properties of mutant Nav1.7 sodium channels in a painful inherited neuropathy. *J Neurosci* **24**, 8232-8236 (2004). <https://doi.org/10.1523/JNEUROSCI.2695-04.2004>
- 16 Nassar, M. A. et al. Nociceptor-specific gene deletion reveals a major role for Nav1.7 (PN1) in acute and inflammatory pain. *Proceedings of the National Academy of Sciences of the United States of America* **101**, 12706-12711 (2004). <https://doi.org/10.1073/pnas.0404915101>
- 17 Yang, Y. et al. Mutations in SCN9A, encoding a sodium channel alpha subunit, in patients with primary erythermalgia. *Journal of medical genetics* **41**, 171-174 (2004).
- 18 Shen, H., Liu, D., Wu, K., Lei, J. & Yan, N. Structures of human Nav1.7 channel in complex with auxiliary subunits and animal toxins. *Science (New York, N.Y)* **363**, 1303-1308 (2019). <https://doi.org/10.1126/science.aaw2493>

19 Huang, G. *et al.* High-resolution structures of human Na(v)1.7 reveal gating modulation through α - π helical transition of S6(IV). *Cell Rep* **39**, 110735 (2022). <https://doi.org/10.1016/j.celrep.2022.110735>

20 Zhang, J. *et al.* Structural basis for Na(V)1.7 inhibition by pore blockers. *Nat Struct Mol Biol* **29**, 1208-1216 (2022). <https://doi.org/10.1038/s41594-022-00860-1>

21 Wu, Q. *et al.* Structural mapping of Na(v)1.7 antagonists. *Nature communications* **14**, 3224 (2023). <https://doi.org/10.1038/s41467-023-38942-3>

22 Huang, J. *et al.* Cannabidiol inhibits Na(v) channels through two distinct binding sites. *Nature communications* **14**, 3613 (2023). <https://doi.org/10.1038/s41467-023-39307-6>

23 Huang, J., Fan, X., Jin, X., Teng, L. & Yan, N. Dual-pocket inhibition of Na(v) channels by the antiepileptic drug lamotrigine. *Proceedings of the National Academy of Sciences of the United States of America* **120**, e2309773120 (2023). <https://doi.org/10.1073/pnas.2309773120>

24 Sutro, J. B. Kinetics of veratridine action on Na channels of skeletal muscle. *The Journal of general physiology* **87**, 1-24 (1986). <https://doi.org/10.1085/jgp.87.1.1>

25 Leibowitz, M. D., Sutro, J. B. & Hille, B. Voltage-dependent gating of veratridine-modified Na channels. *The Journal of general physiology* **87**, 25-46 (1986). <https://doi.org/10.1085/jgp.87.1.25>

26 Ulbricht, W. The effect of veratridine on excitable membranes of nerve and muscle. *Ergeb Physiol* **61**, 18-71 (1969). <https://doi.org/10.1007/BFb0111446>

27 Zhang, X. Y., Bi, R. Y., Zhang, P. & Gan, Y. H. Veratridine modifies the gating of human voltage-gated sodium channel Nav1.7. *Acta Pharmacol Sin* **39**, 1716-1724 (2018). <https://doi.org/10.1038/s41401-018-0065-z>

28 DeLano, W. L. The PyMOL Molecular Graphics System. *on World Wide Web* <http://www.pymol.org> (2002).

29 Fan, X. *et al.* Phrixotoxin-3 binds to three distinct antagonistic sites on human Na(v)1.6. *Cell research* **35**, 610-613 (2025). <https://doi.org/10.1038/s41422-025-01141-4>

30 Weiss, R. E. & Horn, R. Functional differences between two classes of sodium channels in developing rat skeletal muscle. *Science* **233**, 361-364 (1986).

31 Liu, Y., Bassetto, C. A. Z., Jr., Pinto, B. I. & Bezanilla, F. A mechanistic reinterpretation of fast inactivation in voltage-gated Na(+) channels. *Nature communications* **14**, 5072 (2023). <https://doi.org/10.1038/s41467-023-40514-4>

32 Wang, G., Dugas, M., Armah, B. I. & Honerjäger, P. Sodium channel comodification with full activator reveals veratridine reaction dynamics. *Molecular pharmacology* **37**, 144-148 (1990).

33 Barnes, S. & Hille, B. Veratridine modifies open sodium channels. *The Journal of general physiology* **91**, 421-443 (1988).

34 Shen, H. *et al.* Structural basis for the modulation of voltage-gated sodium channels by animal toxins. *Science (New York, N.Y)* **362** (2018). <https://doi.org/10.1126/science.aau2596>

35 Gao, S. *et al.* Structural basis for human Ca(v)1.2 inhibition by multiple drugs and the neurotoxin calciseptine. *Cell* **186**, 5363-5374.e5316 (2023). <https://doi.org/10.1016/j.cell.2023.10.007>

36 Han, D., Tan, H., Sun, C. & Li, G. Dysfunctional Nav1.5 channels due to SCN5A mutations. *Experimental Biology and Medicine* **243**, 852-863 (2018).

37 Gamal El-Din, T. M. When the Gates Swing Open Only: Arrhythmia Mutations That Target the Fast Inactivation Gate of Nav1.5. *Cells* **11**, 3714 (2022).

38 Hu, R.-M. *et al.* Mexiletine rescues a mixed biophysical phenotype of the cardiac sodium channel arising from the SCN5A mutation, N406K, found in LQT3 patients. *Channels* **12**, 176-186 (2018).

39 Itoh, H., Shimizu, M., Takata, S., Mabuchi, H. & Imoto, K. A novel missense mutation in the SCN5A gene associated with Brugada syndrome bidirectionally affecting blocking actions of antiarrhythmic drugs. *Journal of cardiovascular electrophysiology* **16**, 486-493 (2005).

40 Huang, H., Priori, S. G., Napolitano, C., O'Leary, M. E. & Chahine, M. Y1767C, a novel SCN5A mutation, induces a persistent Na⁺ current and potentiates ranolazine inhibition of Nav1.5 channels. *American Journal of Physiology-Heart and Circulatory Physiology* **300**, H288-H299 (2011).

41 Clancy, C. E., Tateyama, M., Liu, H., Wehrens, X. H. & Kass, R. S. Non-equilibrium gating in cardiac Na⁺ channels: an original mechanism of arrhythmia. *Circulation* **107**, 2233-2237 (2003).

42 Meng, E. C., Pettersen, E. F., Couch, G. S., Huang, C. C. & Ferrin, T. E. Tools for integrated sequence-structure analysis with UCSF Chimera. *BMC Bioinformatics* **7**, 339 (2006).
<https://doi.org/10.1186/1471-2105-7-339>

43 Smart, O. S., Neduvvelil, J. G., Wang, X., Wallace, B. A. & Sansom, M. S. HOLE: a program for the analysis of the pore dimensions of ion channel structural models. *J Mol Graph* **14**, 354-360, 376 (1996). [https://doi.org/10.1016/s0263-7855\(97\)00009-x](https://doi.org/10.1016/s0263-7855(97)00009-x)

44 Li, Z. *et al.* Structure of human Na(v)1.5 reveals the fast inactivation-related segments as a mutational hotspot for the long QT syndrome. *Proc Natl Acad Sci U S A* **118** (2021).
<https://doi.org/10.1073/pnas.2100069118>

45 Huang, X. *et al.* Structural basis for high-voltage activation and subtype-specific inhibition of human Na(v)1.8. *Proc Natl Acad Sci U S A* **119**, e2208211119 (2022).
<https://doi.org/10.1073/pnas.2208211119>

46 Fan, X., Huang, J., Jin, X. & Yan, N. Cryo-EM structure of human voltage-gated sodium channel Na(v)1.6. *Proc Natl Acad Sci U S A* **120**, e2220578120 (2023).
<https://doi.org/10.1073/pnas.2220578120>

47 Tegunov, D. & Cramer, P. Real-time cryo-electron microscopy data preprocessing with Warp. *Nat Methods* **16**, 1146-1152 (2019). <https://doi.org/10.1038/s41592-019-0580-y>

48 Punjani, A., Rubinstein, J. L., Fleet, D. J. & Brubaker, M. A. cryoSPARC: algorithms for rapid unsupervised cryo-EM structure determination. *Nat Methods* **14**, 290-296 (2017).
<https://doi.org/10.1038/nmeth.4169>

49 Emsley, P., Lohkamp, B., Scott, W. G. & Cowtan, K. Features and development of Coot. *Acta Crystallogr D Biol Crystallogr* **66**, 486-501 (2010). <https://doi.org/10.1107/S0907444910007493>

50 Afonine, P. V. *et al.* Towards automated crystallographic structure refinement with phenix.refine. *Acta Crystallogr D Biol Crystallogr* **68**, 352-367 (2012). <https://doi.org/10.1107/S0907444912001308>

51 Croll, T. I. ISOLDE: a physically realistic environment for model building into low-resolution electron-density maps. *Acta Crystallogr D Struct Biol* **74**, 519-530 (2018).
<https://doi.org/10.1107/S2059798318002425>

52 Jo, S., Kim, T., Iyer, V. G. & Im, W. CHARMM-GUI: A web-based graphical user interface for CHARMM. *Journal of Computational Chemistry* **29**, 1859-1865 (2008).
<https://doi.org/https://doi.org/10.1002/jcc.20945>

53 Abraham, M. J. *et al.* GROMACS: High performance molecular simulations through multi-level parallelism from laptops to supercomputers. *SoftwareX* **1-2**, 19-25 (2015).
<https://doi.org:https://doi.org/10.1016/j.softx.2015.06.001>

54 Huang, J. *et al.* CHARMM36m: an improved force field for folded and intrinsically disordered proteins. *Nature Methods* **14**, 71-73 (2017). <https://doi.org:10.1038/nmeth.4067>

55 Bussi, G., Donadio, D. & Parrinello, M. Canonical sampling through velocity rescaling. *The Journal of chemical physics* **126**, 014101 (2007). <https://doi.org:10.1063/1.2408420>

56 Parrinello, M. & Rahman, A. Polymorphic transitions in single crystals: A new molecular dynamics method. *Journal of Applied Physics* **52**, 7182-7190 (1981). <https://doi.org:10.1063/1.328693>

57 Darden, T., York, D. & Pedersen, L. Particle mesh Ewald: An N·log(N) method for Ewald sums in large systems. *The Journal of Chemical Physics* **98**, 10089-10092 (1993).
<https://doi.org:10.1063/1.464397>

58 Hess, B., Bekker, H., Berendsen, H. J. C. & Fraaije, J. G. E. M. LINCS: A linear constraint solver for molecular simulations. *Journal of Computational Chemistry* **18**, 1463-1472 (1997).
[https://doi.org:https://doi.org/10.1002/\(SICI\)1096-987X\(199709\)18:12<1463::AID-JCC4>3.0.CO;2-H](https://doi.org:https://doi.org/10.1002/(SICI)1096-987X(199709)18:12<1463::AID-JCC4>3.0.CO;2-H)

59 Michaud-Agrawal, N., Denning, E. J., Woolf, T. B. & Beckstein, O. MDAnalysis: A toolkit for the analysis of molecular dynamics simulations. *Journal of Computational Chemistry* **32**, 2319-2327 (2011). <https://doi.org:https://doi.org/10.1002/jcc.21787>